Additive Manufacturing 37 (2021) 101618

Contents lists available at ScienceDirect

Additive Manufacturing

journal homepage: www.elsevier.com/locate/addma

Full Length Article

Printability and performance of 3D conductive graphite structures

Roneisha Haney [a], Phong Tran [b,c], Edward B. Trigg [d], Hilmar Koerner [d], Tarik Dickens [b,c], Subramanian Ramakrishnan [a,*]

[a] Department of Chemical and Biomedical Engineering, FAMU-FSU College of Engineering, 2525 Pottsdamer St., Tallahassee, FL, 32310, USA
[b] Department of Industrial and Manufacturing Engineering, FAMU-FSU College of Engineering, 2525 Pottsdamer St., Tallahassee, FL, 32310, USA
[c] High-Performance Material Institute, 2005 Levy Ave., Tallahassee, FL, 32310, USA
[d] Air Force Research Laboratory, Wright-Patterson AFB, OH, 45433, USA

ARTICLE INFO

Keywords:
3D printing
Direct ink writing
Graphene nanoplatelets
Rheology
Complex fluids
Conductive inks

ABSTRACT

Direct ink writing (DIW) of graphite-epoxy composites has gained significant importance in a number of applications in fabricating highly conductive free-standing 3D structures. Processing of the composite inks, which consist of highly loaded graphene nanoplatelets, first involves a detailed understanding of the underlying rheological properties. However, little is known about the effect of processing/print parameters, e.g., print speed has on the orientation of such 2D particles during the printing process and how this subsequently influences the macroscopic properties of the final cured composite. In this work, inks with solid loadings of 7−18 wt% were dispersed into a low viscosity epoxy resin (EPON 862) to form a shear thinning, viscoelastic material. The optimal GNP loading for printing is determined through rheological measurements, and the electrical properties are measured as a function of particle concentration and print speed. The results show a sharp increase in conductivity by a factor of ten as the print speed is increased from 5 to 40 mm/s, and all printed samples had conductivities higher than 10^{-3} S/cm. We attribute this change in conductivity to the shear stresses generated during the deposition of the ink, resulting in a shift in the orientation of the 2D platelet-like fillers. Such results showcase the ability to tune the electrical properties of a printed structure with a constant loading of filler. The present work helps develop design rules for processing of graphene-based 3D structures with enhanced properties (electrical) using additive manufacturing. We envision the use of such structures in a number of applications such as thermal interface materials, shielding materials for electronic devices, and light-emitting devices, to name a few.

1. Introduction

While composites are not a new concept, recent advancements in composite technology are changing the way these materials are designed and manufactured [1,2]. The wide range of matrix-filler combinations available allows for versatility in their properties, enabling them to be applied in the development of several functional materials and devices. Composite materials are often matched to a specific application, and by carefully choosing the reinforcement material and loading, the composite can be tailored to meet specific requirements. Graphene nanoplatelets (GNPs) are ideally suited as a filler in composites due to its aspect ratio (~ 600) [3] and excellent conductive properties (thermal and electrical) [4–6]. Epoxy resins are well known for their exceptional performance properties (thermal stability, mechanical strength, and solvent resistance). They are of particular interest in additive manufacturing (AM) due to their flexibility and ease of processing [7]. The combination of epoxy resins and GNPs is of interest in several applications such as thermal interface materials [8], heat sinks [9], and electromagnetic shielding materials [6]. The properties of the composites in such applications depend upon (i) the properties of the nanofiller, (ii) the concentration of the nanofillers, (iii) the orientation of the nanofillers inside the matrix, and (iv) the manufacturing process of the composite [10]. Understanding the underlying structure-processing-function relationships in such composites is therefore critical in enhancing the performance and hence in improving its range of applicability. [10]. Specifically, the improvement of the processing technique in forming these composites to enhance their performance is of interest. In this study, we take advantage of a facile additive manufacturing technique to fabricate epoxy-GNP composites with enhanced and tunable electrical properties.

* Corresponding author at: 2525 Pottsdamer St., A131, Tallahassee, FL 32310, USA.
E-mail address: srama@eng.famu.fsu.edu (S. Ramakrishnan).

https://doi.org/10.1016/j.addma.2020.101618
Received 5 May 2020; Received in revised form 7 August 2020; Accepted 8 September 2020
Available online 23 September 2020

The first step before 3D printing highly loaded inks lies in a detailed understanding of the underlying rheological properties [11]. The ink needs to have sufficient viscosity and elastic modulus and, when dispensed out of a small nozzle under a controlled flow rate, needs to maintain its structural integrity as multiple layers are being built [12]. DIW of composite-based materials are of interest because they boost the conductivity and strength of the neat polymer being printed, while also allowing for the fabrication of more intricate and multifunctional structures which traditional processing techniques do not entail [13]. Additionally, numerous studies with highly loaded anisotropic fillers have shown that the shear force that is induced on the filler during the DIW printing process causes the nanoparticles to be oriented parallel to the direction of the print [14–17]. How processing affects nanoparticle orientation is thus an open topic that is worthy of investigation. Compton and Lewis reported the fabrication of milled carbon fiber and silicon whisker epoxy-based composites via DIW [18]. The fiber-filled epoxy demonstrated exceptional mechanical properties due to the particles aligning along the direction of the print. Compton and co-workers in a separate study showed that the printing of epoxy-GNP composites resulted in highly toughened 3D structures with anisotropic electrical resistances along the print direction and transverse to the print direction [19]. Recent work has also shown the effect of decreased nozzle diameter and increased print speeds on particle orientation and resultant mechanical properties [20,21]. In addition to the parameters mentioned above, a number of other parameters can be adjusted during the deposition process, including gap height, nozzle speed, extrusion pressure, line width, and nozzle diameter [22–25]. Each of the parameters mentioned can influence both the resolution of the print and the amount of shear that the particles experience during deposition.

Even though graphite/epoxy inks are widely used in 3D printing still, little is known about the effect that shear has on the particle alignment during the deposition process and how this affects the final properties of the composite (electrical conductivity). Therefore, in this paper, we study the effect of printing conditions on the orientation of particles and its resultant effect on macroscopic properties. Our results indicate that in addition to optimizing the ink formulation (via concentration and rheological properties), tuning of processing conditions such as print speed can also be used to manipulate the percolative network of GNPs within the polymer matrix. By increasing the print speed at a fixed concentration, we show that the conductive properties can be significantly enhanced. The change in orientation of the GNPs as a function of print speed is evidenced through XRD measurements and SEM images. This study thus helps develop design rules for the improvement of the overall performance of graphene-based composite structures. Our results provide insight into an important parameter (print speed) that must be considered when optimizing materials utilized in DIW, which is critical in further expanding the applications of these composites.

2. Materials and methods

2.1. Materials

Graphene nanoplatelets in powder form were obtained from XG Sciences. The particles have an average thickness of 6−8 nm and a lateral size of 25 μm coupled with a surface area of 120-150 m^2/g. The epoxy (matrix) consisted of a bisphenol F based epoxy resin (EPON 862) using diethylmethylbenzenediamine (EPIKURE W) as the curing agent.

2.2. Ink preparation

The composite ink was prepared by dispersing the GNPs into the epoxy matrix and curing agent using high-speed centrifugal mixing (THINKY ARE-310). The weight ratio of the curing agent to epoxy is 26.4:100 [26]. For each formulation, the platelets are mixed in small increments (2000 RPMs for 2 min and degassed at 2200 RPMs for 2 min per increment) to ensure uniform dispersion throughout the epoxy. The inks tested for rheology contained the curing agent. Printing experiments were carried out within 2 h of ink formulations, during which no change of rheology of the formulated ink was observed. The compositions of the ink that were formulated include 7, 9, 11, 13, 14, 15, 17, and 18 wt% GNPs (weight of GNPs/total weight of whole ink formulation).

2.3. Ink rheology

Measurements of the rheological properties were carried out using an Anton Paar MCR 302 rheometer. A 25 mm roughened parallel plate geometry was used as the measuring system. For the flow curves, a shear rate range of 0.01–100 s^{-1} was utilized. Viscoelastic measurements of the storage (G') and loss moduli (G'') were carried out at a frequency of 1 Hz in the linear viscoelastic regime. Yield stresses were determined using an amplitude sweep (strain range 0.01–100%). Lastly, structural evolution tests consisted of experiments performed in 7 intervals sequentially, alternating between oscillation and constant shear. Intervals 1, 3, 5, and 7 are G' vs time in the LVE range at 1 Hz and 0.01 % strain. Intervals 2, 4, and 6 apply constant shear for 5 s at 50 s^{-1}. Interval 1 is G' vs time before beginning of shear (initial state) and all the other remaining odd-numbered intervals monitors the recovery after shear. The temperature was kept fixed at 25 °C for all measurements.

2.4. Direct ink writing

For the printing process, the ink is first loaded into a 3cc syringe and centrifuged (2000 rpm, 5 min) using a Thinky ARE 310 planetary mixer to remove air bubbles. Printing is then accomplished using the nScrypt 3Dn-300 printer equipped with Nordson dispensing system (Ultimus V). The inks are printed using a 410 μm tapered tip to prevent clogging during printing with a gap size of 300 μm. The structures were printed at speeds varying from 5−40 mm/s with pressures ranging from 480 to 960 kPa. The pressure was adjusted to keep a constant line width (450 μm) at each printing speed. Customized gcode was written to print the different structures and the printed parts were cured at 200 °C for 3 h after which they were removed from the underlying substrate for other measurements.

2.5. Electrical conductivity

The electrical resistivity was measured according to ASTM D257 at ~ 25 °C (room temperature). Each printed and cast sample was machined and polished to yield $10 \times 10 \times 1$ mm rectangular specimen, with loadings of GNP varying from 7−15 wt%. Minimization of the contact resistance between the probe and the sample was achieved by applying silver paste across the surface area of each sample. The surface area (reference Fig. 1A) that the silver paste was applied to depends upon the desired region of interest. In this study, the two areas included are-parallel to the direction of print, where the silver paste is applied to the x-z surface (denoted red in Fig. 1A) and transverse to the direction of print, where the silver paste is applied to the y-z surfaces (denoted green in Fig. 1A). The silver paste was allowed to dry for at least 1 h at 25 °C (room temperature) before resistance measurements. Measurements of resistances were done using a two probe test in which a constant voltage was applied using a Keithley 2400 source meter.

The electrical resistance of each specimen was then measured along two different directions (parallel and transverse to the direction of print). Electrical resistivity (ρ) (inverse of electrical conductivity) can be calculated as follows for each direction:

$$\rho_{||} = RA_{xz}/L_y \quad (1)$$

$$\rho_{\perp} = RA_{yz}/L_x \quad (2)$$

Where A, L, and R are the cross-sectional area, the distance between the electrodes (in the sample), and the measured resistance, respectively.

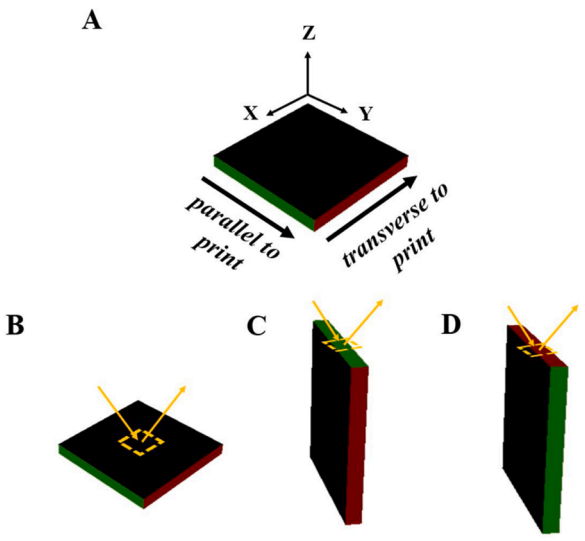

Fig. 1. (A) Schematic of the printed epoxy-GNP structures. (B-D) Schematic of the XRD measurements on different faces, which allows for probing the orientation of platelets with a surface plane parallel to the (B) x-y surface (black), (C) y-z surface(green), and (D) x-z surface(red). The yellow arrows represent the incident and reflected X-ray beam. (For interpretation of the references to colour in this figure legend, the reader is referred to the web version of this article).

2.6. X-ray diffraction

X-ray diffraction (XRD) measurements were carried out using a Rigaku Smartlab instrument. The instrument utilizes Cu Kα radiation (λ =0.154 nm, 40 mA, 40 kV) operating in parallel beam reflection mode. The 2θ range was 10°<2θ<30° with a step size of 0.04°. A schematic of the experimental set up is shown in Fig. 1B–D. A sample height calibration is performed prior to the start of the experiment to ensure that the surface of the sample is probed for each configuration. In an individual measurement, the beam size is 10 mm x 1 mm (width x height). The measurements were repeated at the two faces of each sample for two different samples at the same condition (4 total measurements). Since the amount of resin (epoxy) is constant across all samples at 67 wt% and the epoxy peak occurs at 2θ = 19.04° - we normalize to the intensity of the epoxy amorphous halo.

2.7. Scanning Electron microscopy

The morphology of the top/x-y surface (denoted black in Fig. 1A) and fractured y-z surface (denoted green in Fig. 1A) of the printed specimens was examined using scanning electron microscopy (SEM, Helios G4 UC). Carbon adhesive tape was used to glue 1 mm x 1 mm x 1 mm samples onto aluminum holders. Imaging contrast was improved by depositing ~ 2 nm layer of platinum on the sample surface. Imaging was carried out using an accelerating voltage of 10 kV (high vacuum) at a working distance of 10 mm.

3. Results and discussion

3.1. Rheology and printability

Tuning rheological properties of the inks before printing is key to final composite performance – the inks need to be shear thinning to enable extrusion while at the same time have sufficient viscoelasticity to enable rapid recovery after deposition. A printable material needs to be optimized to have low viscosity during extrusion (shear thinning) and sufficient modulus after being printed (viscoelastic & demonstrate rapid recovery). The shear-thinning properties of the inks are evidenced through rotational measurements (Fig. 2A), the viscoelasticity is shown through the amplitude sweep (Fig. 2B), and recovery of the inks under similar conditions experienced during printing is demonstrated after a structural evolution test (Fig. 2C). After determining the optimal loading of GNPs for printing, the concentration of GNPs can be fixed, and the remaining experiments can be carried out. Fig. 2A is a plot of viscosity (steady shear) as a function of shear rate for the different samples studied in this work. During DIW, Compton and co-workers showed that materials experience a shear rate of ~50 s^{-1} in the nozzle [18]. Hence, flow curves in this work were measured in the shear rate range of 0.01−100 s^{-1}. The viscosity of a shear-thinning fluid loaded with particles can be modeled using the Power Law [24]:

$$\eta = K\dot{\gamma}^{n-1} \quad (3)$$

Where η is the viscosity (Pa s), $\dot{\gamma}$ is the shear rate (s^{-1}), K is a shear-thinning coefficient, and n is a power-law exponent. The values of n are close to 1 for Newtonian fluids, 0.6 for weakly shear-thinning fluids, and 0.2 for highly shear-thinning materials [24]. For the neat epoxy, the power-law model showed Newtonian behavior ($n = 0.99$). As the GNP loading is increased, we observe an increase in shear-thinning, non-Newtonian behavior, as demonstrated through the change of the shear-thinning coefficients. This shear-thinning behavior is necessary to ensure that the material can flow with limited restriction through the nozzle (i.e., zero clogging), yet still exhibit a relatively high viscosity when the shear stress is removed as it exits the nozzle.

Fig. 2B shows the results of G' (solid squares) and G'' (hollow squares) from the amplitude sweep. The 11 wt% formulation shows liquid-like behavior (G''>G'), despite its shear-thinning characteristics shown in Fig. 2A. It is important to reiterate that for a material to be used for DIW, both criteria (shear thinning and viscoelastic behavior) must be met. A printable material must show solid-like behavior (G'>G'') and exhibit a yield stress (τ_y - cross over of G' and G''). As can be seen in Fig. 2B and S1, for loadings >13 wt%, G'>G'' and a yield stress is present, thus clearly delineating samples that can be printed. The 14 wt% sample exhibits a plateau G' around 1500 Pa (Fig. S1 in Supplement) and a yield stress around 1 Pa. With the addition of more GNPs (15 wt%), both G' and τ_y increased significantly to near 25,000 Pa and 22 Pa, respectively. When the ink is extruded through the nozzle (shear stresses > τ_y), G'' (liquid behavior) dominates, allowing for ease of flow of the material. On the other hand, when the ink leaves the nozzle, the recovery of high G' values should help retain the shape of the printed specimen.

Fig. 2C further supports this claim with a structural evolution test of the 15 wt% sample. Interval 1 gives G' as a function of time for the material at rest (initial state). The even intervals reveal G' under shear (50 s^{-1} as experienced during extrusion), and all remaining odd intervals detail the elastic modulus of the ink after the stoppage of shear (or after printing is stopped). Initially (Interval 1), the inks exhibit a large storage modulus indicating a solid-like structure. After shear, the G' recovers to the same G' value of the initial structure at rest (to 96 % of final plateau value within three minutes). The recovery of G' to an equivalent modulus showcases the robustness of the material. Since the modulus recovers (within a factor of 1.1) to the original value, we also hypothesize that the shear used in the rheology experiments and during 3D printing is not sufficient to cause exfoliation. This is also confirmed by reports in the literature that state that exfoliation of graphene can only occur at shear rates greater than 10^4 s^{-1} [27].

The effect of rheological percolation on modulus can also be seen in Fig. 3, where G' is measured as a function of oscillation frequency (Fig. 3A) and GNP content (Fig. 3B). In Fig. 3A, the slope of G' decreases significantly from 11 wt% to 13 wt%. This is evidence that the modulus is becoming less dependent on frequency, indicating the formation of a solid-like structure with long relaxation times (after percolation). Fig. 3B is a plot of G' (in the LVE range and a frequency of 1 Hz) as a function of GNP concentration, and as can be seen, between 11 wt% and 13 wt%, there is a rapid jump in G', indicating percolation. As the concentration

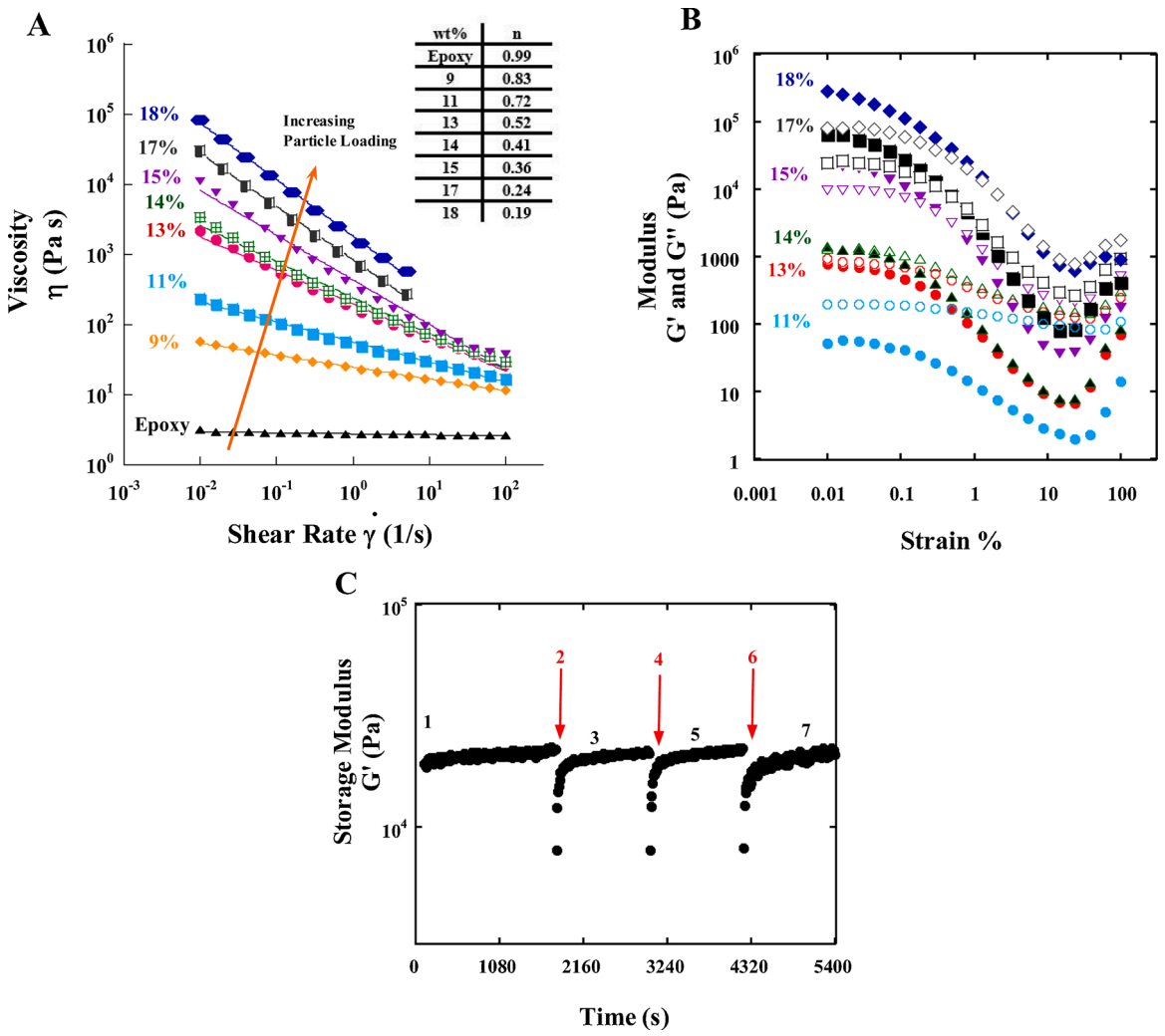

Fig. 2. Rheological measurements of the epoxy-GNP inks (A) Viscosity as a function of shear rate for different GNP loadings. Viscosity varies in a power-law manner with shear rate, where power-law exponents are shown in the figure. (B) Elastic modulus (G', solid squares) and loss modulus (G", hollow squares) as a function of applied strain (amplitude sweep) at 1 Hz (C) Recovery of elastic modulus after a constant shear ($50s^{-1}$, 5 s) of the 15 wt% GNP sample, where Interval 1 is the ink "at rest," all even intervals detail sample under constant shear. The remaining odd intervals show the recovery of G'.

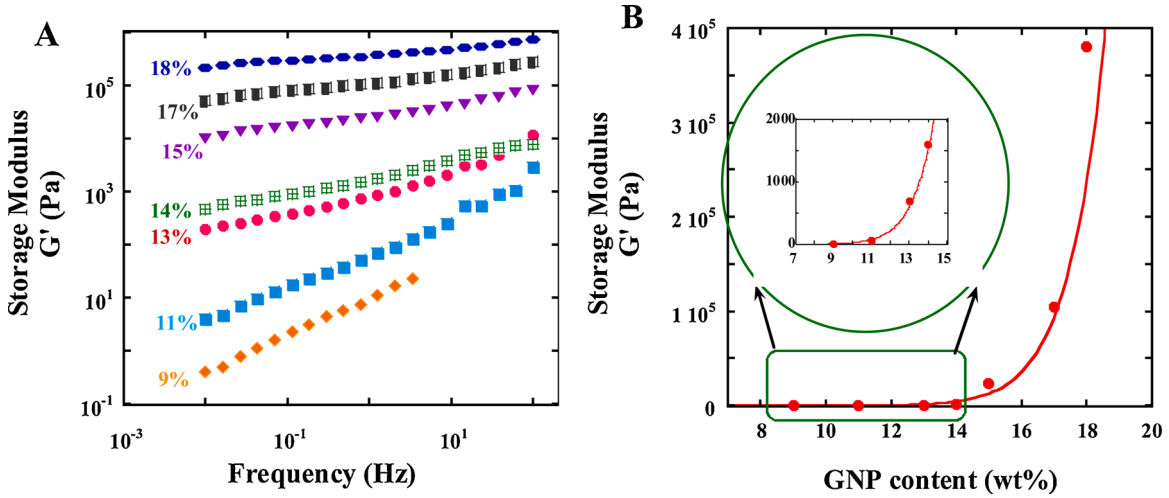

Fig. 3. Rheological measurements to showcase the percolation threshold. Fig. 3A shows G' as a function of frequency (0.01-100 Hz) for various GNP concentrations. Fig. 3B is a plot of storage modulus (G') at 1 Hz as a function of particle concentration (black-below percolation, blue-above percolation). The inset gives the moduli till a weight percentage of 14 %. Percolation is identified by a rapid jump in the elastic modulus above a critical concentration. The red line is a power-law fit to the experimental data and is to guide the eye. (For interpretation of the references to colour in this figure legend, the reader is referred to the web version of this article).

is increased, the fillers form a percolative network that can withstand stress and allow for enhancement of macroscopic properties (strength and conductivity) [28]. The 13 wt% sample, which is close to the percolation boundary, is very sensitive to the oscillation strain % used in the experiment (0.03 %). Hence for printing, the particle concentration needs to be above 13 % to obtain a self-sustaining network.

Fig. 4 demonstrates the printability of the material and showcases its relationship between the rheological properties, where tan δ is the ratio of G" and G', thus signifying the ability of the structure to bear stress. The three concentrations shown in Fig. 4 were chosen based on results from the rheological study, where 11 wt% is below percolation and expected to show liquid-like behavior (tan $\delta > 1$), 13 wt% is close to the onset of percolation (tan $\delta \approx 1$), and 15 wt% lies above the percolation concentration (tan $\delta < 1$) and has strong viscoelastic properties. For each formulation (11, 13, 15 wt%), the pressure was adjusted to keep a constant line width at a speed of 40 mm/s. The g-code script was set to print a 10 mm x 10 mm hollow square with a total of 7 layers. As shown in the figure, the 11 wt% formulation does not hold its shape due to the high tan δ value. At the onset of percolation, the 13 wt% formulation can withstand stress and form a stable structure up to 6 layers but collapses upon the addition of more layers. Finally, above the percolation threshold, the 15 wt% formulation demonstrated excellent printability – all layers could be printed without the collapse of the structure. This study shows a direct relationship between the information obtained from the rheological studies and thus provides insight into the proper ink formulation necessary to build and print the composite structures needed to carry out the remaining tests within this study.

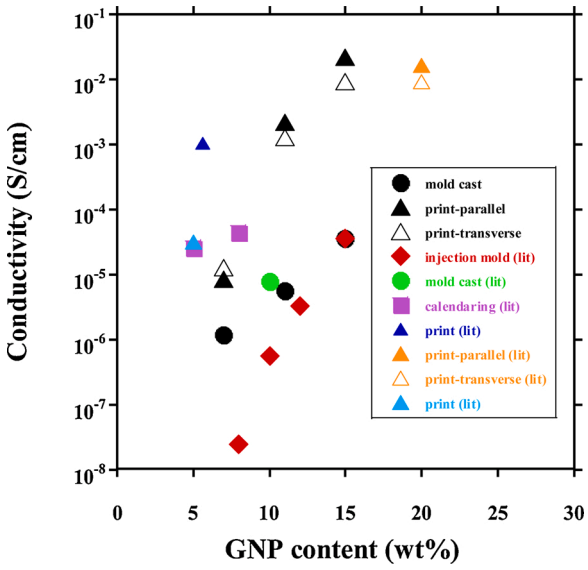

Fig. 5. Electrical conductivity as a function of GNP content for printed and mold cast samples in current work (all samples in current work are in black color - mold cast ●, parallel to print direction▲, transverse to print direction △). Reported values in the literature of 3D printed conductive polymer composites (▲ [39], ▲ [19], ▲ [40]) and traditionally manufactured conductive polymer composites (injection mold ◆ [30], calendaring ■ [41], and mold cast ● [32]).

3.2. Electrical conductivity

The anisotropic nature of graphene particles coupled with excellent thermal and electrical properties makes it a prime candidate for the production of conductive polymer composites [29]. A number of studies in literature have demonstrated the applicability of these conductive materials [30–34] in manufacture of batteries [35], shielding materials [36], coatings [37] (corrosion resistant), and light-emitting diodes [38].

The electrical conductivities of mold-cast (●) and printed samples (▲, □) as a function of GNP content (7, 11, 15 wt%) for this study is shown in Fig. 5. For each formulation (7, 11, 15 wt%), the pressure was adjusted to keep a constant line width at a speed of 40 mm/s. The conductivities of the printed samples are measured in parallel and transverse directions (Fig. 1A). As the GNP content increases from 7 wt% to 15 wt%, the conductivity increases by a factor of 2760. We attribute this to the formation of a percolated network of particles in the epoxy matrix. Additionally, literature data on the conductivity of polymer-GNP nanocomposites manufactured via 3D printing (filament printing and DIW) and by other traditional techniques (injection mold [30], mold casting [32], and calendaring [41]) is presented in Fig. 5. The composites that were manufactured via DIW in current work have higher conductivity values than traditional methods of manufacture. For example, the injection-molded samples at a loading of 15 wt% have an electrical conductivity value of 3.58×10^{-5} S/cm, where at the same

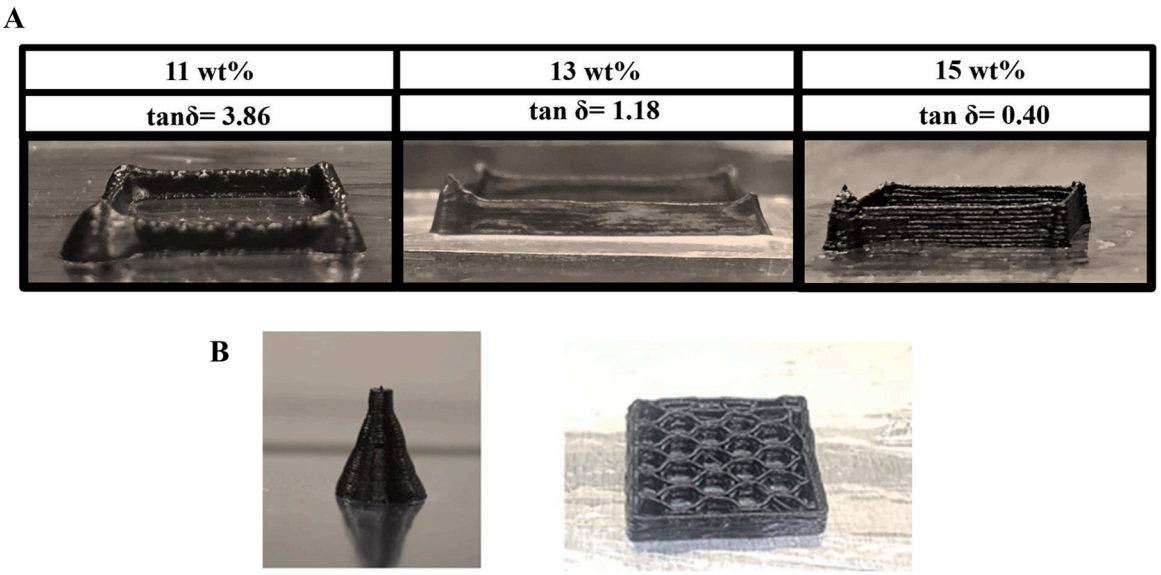

Fig. 4. (A) Demonstration of shape retention after printing, where 7-layer, hollow square structures are printed via direct ink writing at 11, 13, and 15 wt% loadings of GNPs. The printing speed is 40 mm/s. The tan δ values are taken from rheology experiments (Fig. 2) at a frequency of oscillation of 1 Hz. (B) Picture of a funnel and honeycomb structure printed with the 15 wt% ink.

filler loading for a composite processed via DIW, we report a conductivity value of 2.22×10^{-2} S/cm – an enhancement of 619. In literature there are a number of studies that have taken graphene (which has higher conductivity) formulated inks/filaments and 3D printed composites. In a study done by Wu et al. (exfoliated graphene and polyborosiloxane [40]), the performance of their 3D printed structures is slightly higher than our reported values at 7 wt%, which is due to the use of exfoliated of graphene vs. multi-layer graphene or GNPs. Similarly, in a study done by Wei et al., functionalized graphene oxide (GO) is dispersed into acrylonitrile-butadiene-styrene to 3D print conductive structures [39]. At GO loadings greater than 5.6 wt%, the nozzle clogged, limiting the researchers to only report the shown values. Compton and co-workers reported the fabrication of electrically conducting epoxy-based GNP structures [19]. We report higher (factor of 1.4) conductivity values at 15 wt%, compared to a loading of 20 wt% in their study. In our study, by tuning the print parameters – by using a smaller nozzle and faster print speed, we were able to achieve the desired results at a lower loading. The changes in electrical performance when comparing the two studies highlight the importance of print settings and conditions on the overall performance of the final structure. Lastly, our electrical performance is almost three orders of magnitude higher than values reported with traditional methods and shows a clear advantage of using DIW as a manufacturing process.

3.3. *Effect of print speed on the conductivity and orientation of GNPs*

Several studies have shown that during DIW, the nozzle size, print speed, and extrusion pressure can be adjusted to control the width of the printed line [24,25]. The feature size and resolution is an essential factor to consider during printing. However, it should also be noted that the alteration of these parameters results in a change of shear forces that the particles experience during the printing process and hence has an effect on their alignment. As reported in the previous section and in agreement with similar printing-related literature [18,19,22], there is a dramatic change in bulk properties when comparing the performance of mold-cast samples to printed samples. Numerous studies with highly anisotropic rod-like fillers have shown that the shear force that is induced on the filler during printing causes these nanoparticles to be oriented parallel to the direction of the print [42,43]. This change in the alignment of the nanoparticles within the printed structure then results in an enhancement in the conductive properties (and other bulk properties) of the material. In order to examine the extent to which shear-induced forces can alter the orientation of fillers during printing, we studied the effect of print speed on electrical conductivity.

The print speed for this portion of the study was increased from 5 to 40 mm/s (with a constant GNP loading of 15 wt%), and the pressure was adjusted to keep a constant line width of ~550 μm. The electrical conductivity was measured in two different directions with respect to the direction of print - parallel and transverse. In Fig. 6, we show that as the print speed is increased during the DIW process, we observe a change in electrical conductivity (parallel to the print direction) by a factor of ~ 2.52. The sample that was printed at 5 mm/s shows a conductivity value of 8.82×10^{-3} S/cm, which is still higher than the cast sample at the same loading (3.59×10^{-5} S/cm). When the print speed is increased to 40 mm/s, we observe an even higher value of conductivity at 2.22×10^{-2} S/cm. The standard deviation across five different printed samples is depicted in the error bars, as shown in the figure. The error can be attributed to voids (due to entrapment of air), which are commonly formed during ink preparation and the DIW process. Nevertheless, these results demonstrate that the shear-induced alignment of particles during printing can significantly enhance percolation and hence enhance the bulk properties. Additionally, the conductivity at 40 mm/s parallel to the direction of print is also higher (factor of 2.45) than in the transverse direction. The electrical anisotropy with respect to the two directions reflects the large degree of favored orientation of the GNPs in the direction parallel to the print. These results are in agreement with recent

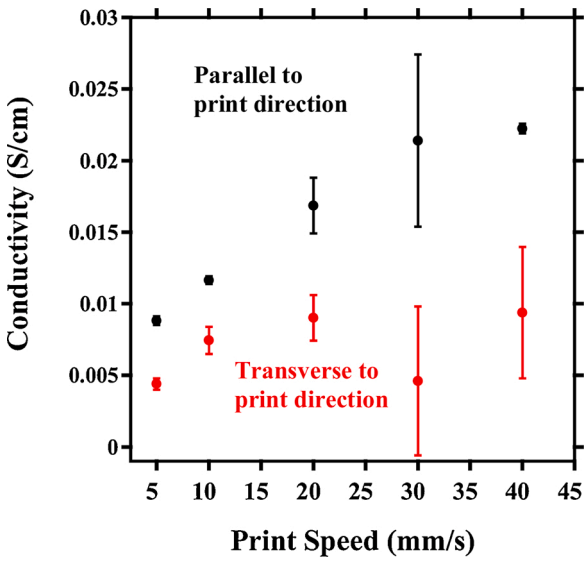

Fig. 6. The electrical conductivity of the printed specimens over a range of print speeds (5-40 mm/s) at a loading of 15 wt% GNP, in the direction parallel (black) and transverse (red) to the print direction. (For interpretation of the references to colour in this figure legend, the reader is referred to the web version of this article).

work on aligned (by application of an electric field) epoxy-graphene composites by Wu and co-workers who demonstrated the difference in electrical properties along different directions (anisotropic electrical properties) [44].

The reason for this significant change in conductivity during the printing process can be attributed to the shear-induced alignment of the particles while being deposited on the print bed. As the print speed is increased, the amount of shear that the particles experience is also increased, thus influencing the alignment of the fillers. To explain and confirm the change in orientation of the fillers at the different print speeds, XRD measurements were performed along with microscopy (SEM).

Measurement of the intensity of the (002) Bragg peak at ($2\theta = 26.4^\circ$ - graphite basal plane spacing of 0.34 nm) by XRD can be utilized to track the orientation of the platelets [45]. For an in-plane alignment of graphitic platelets, Bragg's equation ($2d\sin\Theta = n\lambda$) is satisfied and causes the formation of a peak at $2\theta = 26.4^\circ$ [46,47]. For an out of plane alignment, the absence of regular planes (parallel to the surface plane) results in a decrease in the intensity at $2\theta = 26.4^\circ$ [36,48]. Fig. 7A–C displays the intensity values obtained from the XRD pattern of printed samples at 15 wt% GNPs, where the maximum peak intensity has been normalized to 1. The peak intensity is plotted as a function of 2θ for different print speeds. Measurements were done on three different surfaces (x-y surface-black, y-z surface-green, x-z surface-red), as shown in the embedded images in the figure.

Fig. 7A is a plot of the intensity with respect to the x-y surface. When the print speed is increased, the intensity of the peak at 26.4° decreases. The change in intensity is due to a change in orientation of the GNPs due to the shear-induced alignment during the deposition process. This induced shear results in the vertical (non-parallel)

alignment of the GNPs with respect to the x-y surface of the sample and hence a reduction of peak intensity with print speed. The results suggest parallel orientation of the platelets (parallel to the x-y surface) at the lower print speed (5 mm/s), as compared to the higher print speed (40 mm/s). Similar decreases in XRD peak intensity (at 26.4°) is seen in the work of Billaud et al., where the application of a magnetic field results in an out of plane alignment of the platelets [35].

To investigate the out of plane alignment at higher speeds, two more XRD measurements on the transverse direction (y-z) and the edge face

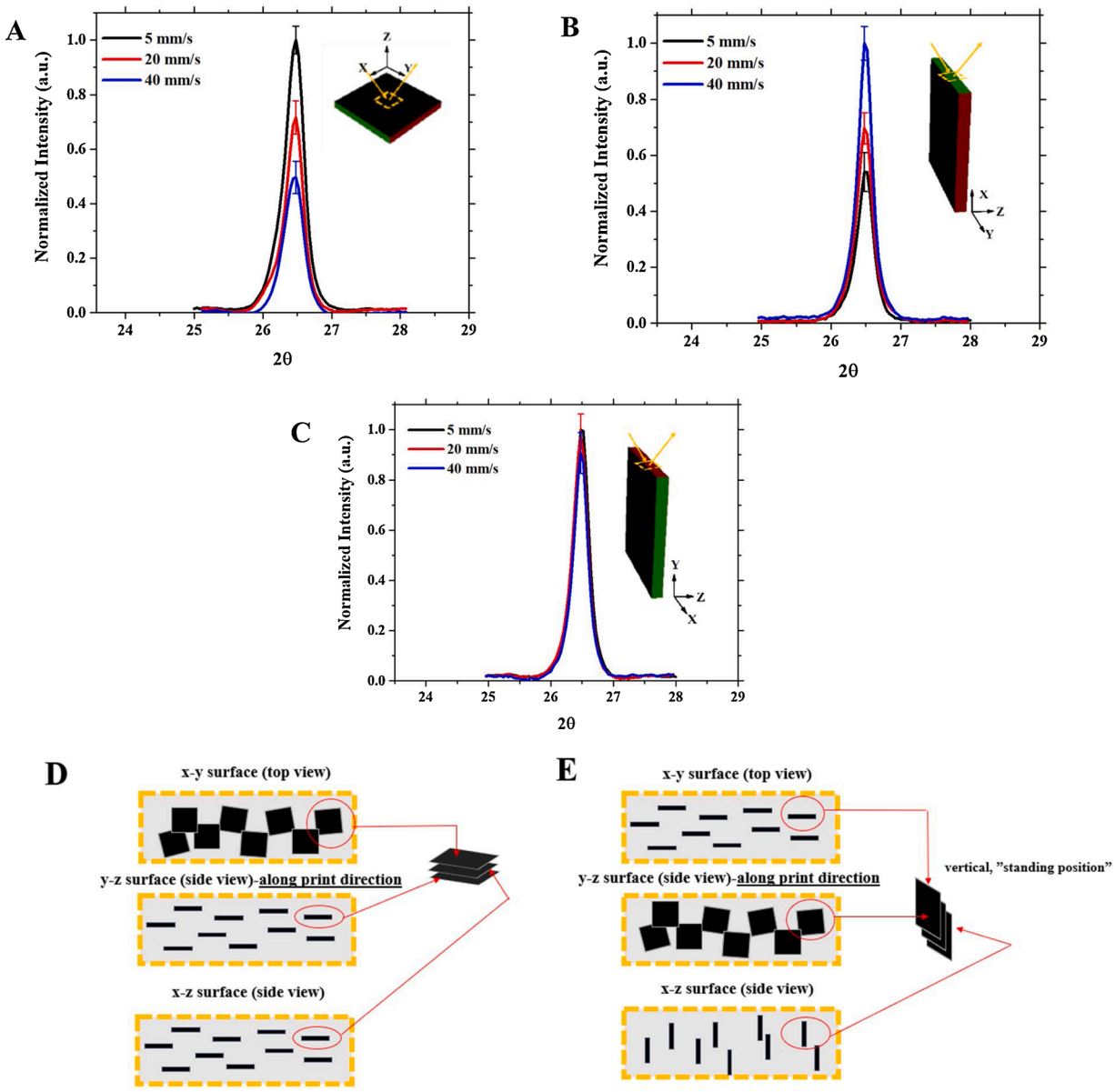

Fig. 7. (A-C) XRD measurement patterns (normalized to 1) of the printed specimens (15 wt% epoxy-GNP) at various print speeds (5, 20, and 40 mm/s) and the corresponding schematics (D, E) of the orientation of the GNPs within the printed specimens at (D) 5 mm/s and (E) 40 mm/s. Measurements are performed across the (A) x-y surface, (B) y-z surface, and (C) x-z surface. The yellow arrows represent the incident and reflected beam. (For interpretation of the references to colour in this figure legend, the reader is referred to the web version of this article).

(x-z) were carried out. Fig. 7B gives the intensity of the peak at 26.4° when measurements were done on the y-z surface (transverse). As can be seen from the figure, the intensity increases systematically as print speed is increased with 40 mm/s print speed giving the highest intensity. This suggests that the platelets orient in a "standing" or vertical position along the y-z surface with their normal along the "x" direction – resulting in increased intensity, which corresponds to basal plane spacing. Finally, in Fig. 7C, we observe no change in intensity as print speed is changed. Based on the previous results from Fig. 7A–B, we expect that if most of the platelets lie in the x-y plane (low print speeds) or lie in the y-z plane (high print speeds), the intensity with respect to the x-z surface should be consistent across all samples due to the absence of the graphitic basal plane when XRD measurements are performed. A schematic of the orientation of the GNPs is given in Fig. 7D–E for the lower and higher printing speeds, respectively. It should be noted that the schematics are an oversimplification and do not include distributions of the nanoparticles away from the ideal direction.

The combined results from the electrical and XRD measurements suggest that maximum performance occurs when the platelets are oriented in the vertical/" standing" position, as shown in Fig. 7E. While "standing" or vertical alignment of anisotropic platelet-shaped particles might intuitively not be expected, there have been several studies that show that the orientation of such 2D particles depends on the amount of shear imposed [49–52]. Kojima et al. measured platelet orientation in a clay-nylon 6 nanocomposite (manufactured via injection mold) [50]. The orientation in this study was found to be a function of the depth of the molded rod with two distinct regions. Near the center of the rod where the particles experience low shear, random orientation was found. Near the surface where particles experience high shear, platelets were oriented parallel to the surface – similar to the orientation we observe at lower print speeds. On the contrary, Okamoto and co-workers observed perpendicular alignment of clay platelets – with the surface normal along the direction of flow (or stretching direction) [51]. We observe a similar orientation in our printed samples as we increase print

speed, where our platelets are orienting in a perpendicular or vertical alignment in the print direction or with respect to the x-y surface. Although this arrangement is counterintuitive, several studies have also observed such perpendicular alignment of anisotropic particles [49,51,52]. The variation in the orientation of the 2D fillers used in the studies mentioned showcases the alignment dependence on the manufacturing method used to process such materials. While the shear-induced changes in orientation of platelet-shaped particles have been studied, the results from this study showcase the ability to continuously change and tune the electrical properties of a single printed road, allowing for the fabrication of printed parts with distinct complex property landscapes.

SEM images (Fig. 8) of the morphology of the printed 15 wt% sample at each print speed are consistent with the results presented in Fig. 7. The images in Fig. 8 highlights the morphology of both the surface (Fig. 8 A, C, and E) and fractured cross-section (Fig. 8B, D, and F) of the composites printed at 5 mm/s (A & D), 20 mm/s (B & E), and 40 mm/s (C & F). The top surface view (x-y surface) of the specimens printed at the higher speed (Fig. 8E) clearly depicts the formation of a percolated network of the filler particles (GNPs) in the direction of print – which is not present at lower print speeds (Fig. 8A). This orientation of the platelets is further confirmed through the fractured cross-sectional view (Fig. 8F), where platelets are aligned parallel to the y-z surface (yellow arrows). Conversely, in Fig. 8B, multi-layered stacked graphite structures are shown (blue arrows), which demonstrates that at lower print speeds, some, if not most, platelets are aligned parallel to the x-y surface. Finally, we observe in the 20 mm/s printed sample (Fig. 8C–D), evidence of platelets aligned both parallel to the x-y surface (blue arrow) and the y-z surface (yellow arrows).

4. Conclusion

In summary, we have investigated epoxy-GNP inks as feedstock for DIW and demonstrated that we can influence and increase the electrical performance of the printed structure not only via the filler content but also the print speed. The rheological properties of the inks are assessed, where we found the rheological percolation threshold to be at ~13 wt%. The printability and electrical properties of the composite are then investigated around and above this value. As expected, below percolation, we observe a non-printable, low-performance composite. Above percolation, at 15 wt%, we obtain a printable composite with high electrical conductivity. Finally, after optimizing the filler content, we show that print speed significantly influences the electrical performance of the printed structure, where we observe an increase in conductivity by a factor of 2.52 at a constant loading of 15 wt% GNPs at a print speed of 40 mm/s. XRD measurements and SEM images confirm the change in the orientation of the platelets at the different print speeds, resulting in changes in the overall performance of the final printed structure. The current findings showcase a simple, cost-effective method to control the orientation of anisotropic particles during printing to allow for the development of enhanced polymeric nanocomposites to be used in a wide variety of applications, such as heat sinks, thermal interface materials, and electronic devices.

Funding

This work was supported by the National Science Foundation award [1735968]. Partial support from NSF award [1623206] is also acknowledged. A portion of this work was performed at the National High Magnetic Field Laboratory, which is supported by the National Science Foundation Cooperative Agreement No. DMR-1644779 and the State of FloridaS. This research was performed while E.B.T. held an NRC Research Associateship award at the Air Force Research Laboratory (Wright-Patterson Air Force Base, Ohio).

CRediT authorship contribution statement

Roneisha Haney: Conceptualization, Methodology, Formal analysis, Data curation, Writing - original draft. **Phong Tran:** Methodology, Formal analysis. **Edward B. Trigg:** Methodology, Writing - review & editing. **Hilmar Koerner:** Methodology, Writing - review & editing. **Tarik Dickens:** Methodology, Writing - review & editing, Formal analysis. **Subramanian Ramakrishnan:** Conceptualization, Formal analysis, Data curation, Funding acquisition, Writing - original draft.

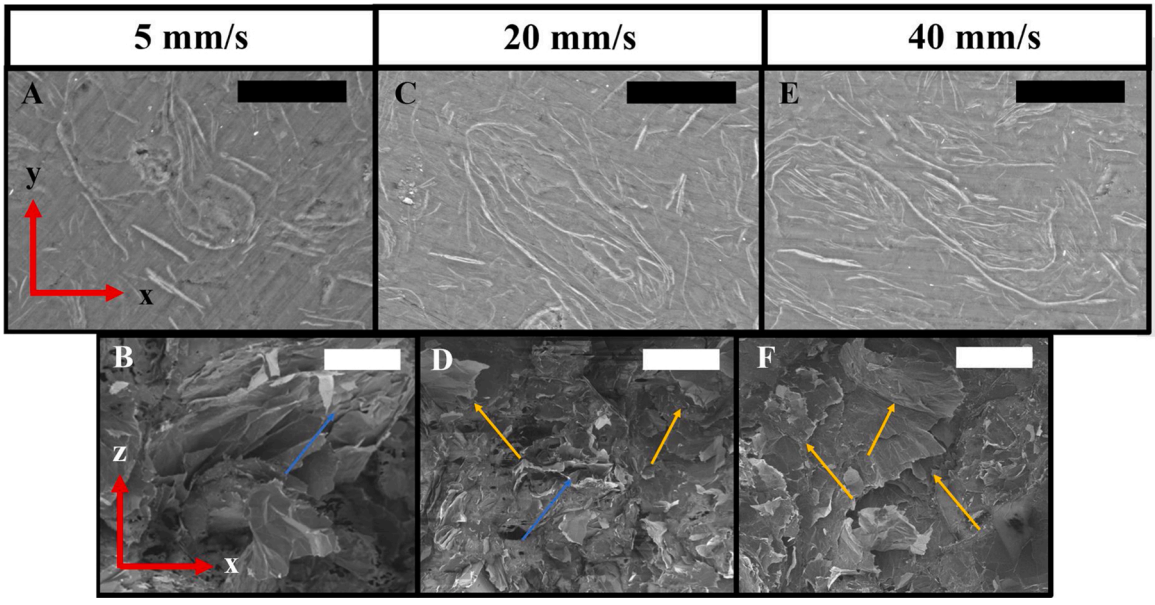

Fig. 8. SEM images (A-F) of the morphology of the printed 15 wt% GNP-epoxy composite structures manufactured using three different print speeds ((A-B) 5 mm/s, (C-D) 20 mm/s, and (E-F) 40 mm/s). Images A, C, and E showcase the morphology of the top surface of the printed structure (x-y surface, scale bar 40 μm). Images B, D, and F showcase the cross-sections of the printed structure along the print direction (y-z surface, scale bar 20 μm). The blue arrows denote platelets aligned parallel x-y surface, and the yellow arrows denote platelets aligned vertically to the x-y surface (parallel to the y-z surface), where x is the printing direction. (For interpretation of the references to colour in this figure legend, the reader is referred to the web version of this article).

Declaration of Competing Interest

The authors report no declarations of interest.

Acknowledgements

R.H and S.R. would like to acknowledge the Air Force Research Laboratory (Wright-Patterson Air Force Base) for the current work.

Appendix A. Supplementary data

Supplementary material related to this article can be found, in the online version, at doi:https://doi.org/10.1016/j.addma.2020.101618.

References

[1] J. Frketic, T. Dickens, S. Ramakrishnan, Automated manufacturing and processing of fiber-reinforced polymer (FRP) composites: an additive review of contemporary and modern techniques for advanced materials manufacturing, Addit. Manuf. 14 (2017) 69–86, https://doi.org/10.1016/j.addma.2017.01.003.
[2] M. Roy, Additive Technology of Soluble Mold Tooling for Embedded Devices in Composite Structures: A Study on Manufactured Tolerances, Florida State University, 2015.
[3] F. Bonaccorso, A. Bartolotta, J. Coleman, C. Backes, 2D-crystal-based functional inks, Adv. Mater. 28 (2016) 6136–6166, https://doi.org/10.1002/adma.201506410.
[4] K. Fu, Y. Wang, C. Yan, Y. Yonggang, Y. Chen, J. Dai, S. Lacey, Y. Wang, J. Wan, T. Li, Z. Wang, Y. Xu, L. Hu, Graphene oxide-based electrode inks for 3D-printed lithium-ion batteries, Adv. Mater. 28 (2016) 2587–2594, https://doi.org/10.1002/adma.201505391.
[5] Z. Chen, C. Xu, C. Ma, W. Ren, H.-M. Cheng, Lightweight and flexible graphene foam composites for high-performance electromagnetic interference shielding, Adv. Mater. 25 (2013) 1296–1300, https://doi.org/10.1002/adma.201204196.
[6] B. Shen, W. Zhai, Z. Wenge, Ultrathin flexible graphene film: an excellent thermal conducting material with efficient EMI shielding, Adv. Funct. Mater. 24 (2014) 4542–4548, https://doi.org/10.1002/adfm.201400079.
[7] L. Tang, C. Weder, Cellulose Whisker/Epoxy resin nanocomposites, ACS Appl. Mater. Interfaces 2 (2010) 1073–1080, https://doi.org/10.1021/am900830h.
[8] A. Yu, P. Ramesh, X. Sun, E. Bekyarova, M.E. Itkis, R.C. Haddon, Enhanced thermal conductivity in a hybrid graphite nanoplatelet – carbon nanotube filler for epoxy composites, Adv. Mater. 20 (2008) 4740–4744, https://doi.org/10.1002/adma.200800401.
[9] N. Nguyen, E. Melamed, J.G. Park, S. Zhang, A. Hao, R. Liang, Direct printing of thermal management device using low-cost composite ink, Macromol. Mater. Eng. 302 (2017) 1700135, https://doi.org/10.1002/mame.201700135.
[10] M. Supova, G. Martynkova, K. Barabaszova, Effect of nanofillers dispersion in polymer matrices: a review, Sci. Adv. Mater. 3 (2011) 1–25, https://doi.org/10.1166/sam.2011.1136.
[11] R. Karyappa, M. Hashimoto, Chocolate-based ink three-dimensional printing (Ci3DP), Sci. Rep. 9 (2019) 14178, https://doi.org/10.1038/s41598-019-50583-5.
[12] H. Elsayed, A. Chmielarz, M. Potoczek, T. Fey, P. Colombo, Direct ink writing of three dimensional Ti2AlC porous structures, Addit. Manuf. 28 (2019) 365–372, https://doi.org/10.1016/j.addma.2019.05.018.
[13] R.D. Farahani, M. Dubé, Printing polymer nanocomposites and composites in three dimensions, Adv. Eng. Mater. 20 (2018) 1700539, https://doi.org/10.1002/adem.201700539.
[14] N. Hmeidat, J. Kemp, B. Compton, High-strength epoxy nanocomposites for 3D printing, Compos. Sci. Technol. 160 (2018), https://doi.org/10.1016/j.compscitech.2018.03.008.
[15] K. Huang, J. Yang, S. Dong, Q. Feng, X. Zhang, Y. Ding, J. Hu, Anisotropy of graphene scaffolds assembled by three-dimensional printing, Carbon 130 (2018) 1–10, https://doi.org/10.1016/j.carbon.2017.12.120.
[16] H.-W. Kang, S.J. Lee, I.K. Ko, C. Kengla, J.J. Yoo, A. Atala, A 3D bioprinting system to produce human-scale tissue constructs with structural integrity, Nat. Biotechnol. 34 (2016) 312–319, https://doi.org/10.1038/nbt.3413.
[17] M. Roy, P. Tran, T. Dickens, B.D. Quaife, Effects of geometry constraints and fiber orientation in field assisted extrusion-based processing, Addit. Manuf. 32 (2020) 101022, https://doi.org/10.1016/j.addma.2019.101022.
[18] B.G. Compton, 3D-Printing of Lightweight Cellular Composites, 2014, https://doi.org/10.1002/adma.201401804 (Accessed 27 July 2020).
[19] B.G. Compton, N.S. Hmeidat, R.C. Pack, M.F. Heres, J.R. Sangoro, Electrical and mechanical properties of 3D-printed graphene-reinforced epoxy, JOM 70 (2018) 292–297, https://doi.org/10.1007/s11837-017-2707-x.
[20] N.S. Hmeidat, R.C. Pack, S.J. Talley, R.B. Moore, B.G. Compton, Mechanical anisotropy in polymer composites produced by material extrusion additive manufacturing, Addit. Manuf. 34 (2020) 101385, https://doi.org/10.1016/j.addma.2020.101385.
[21] J. Peng, T.L. Lin, P. Calvert, Orientation effects in freeformed short-fiber composites, Compos. Part A Appl. Sci. Manuf. 30 (1999) 133–138, https://doi.org/10.1016/S1359-835X(98)00110-9.
[22] J.A. Lewis, J. Smay, J. Stuecker, J. Cesarano, Direct ink writing of three-dimensional ceramic structures, J. Am. Ceram. Soc. 89 (2006) 3599–3609, https://doi.org/10.1111/j.1551-2916.2006.01382.x.
[23] B.M. Rauzan, S.E. Lehman, J.M. McCracken, J. Lee, X.-M. Lin, A. Sandy, S. Narayanan, S.A. Rogers, R.G. Nuzzo, A printing-centric approach to the electrostatic modification of polymer/clay composites for use in 3D direct-ink writing, Adv. Mater. Interfaces 5 (2018) 1701579, https://doi.org/10.1002/admi.201701579.
[24] N. Paxton, W. Smolan, T. Böck, F. Melchels, J. Groll, T. Jungst, Proposal to assess printability of bioinks for extrusion-based bioprinting and evaluation of rheological properties governing bioprintability, Biofabrication 9 (2017) 044107, https://doi.org/10.1088/1758-5090/aa8dd8.
[25] T. Gao, G.J. Gillispie, J.S. Copus, A.K. Pr, Y.-J. Seol, A. Atala, J.J. Yoo, S.J. Lee, Optimization of gelatin-alginate composite bioink printability using rheological parameters: a systematic approach, Biofabrication 10 (2018) 034106, https://doi.org/10.1088/1758-5090/aacdc7.
[26] J.A. King, D.R. Klimek, I. Miskioglu, G.M. Odegard, Mechanical properties of graphene nanoplatelet/epoxy composites, J. Appl. Polym. Sci. 128 (2013) 4217–4223, https://doi.org/10.1002/app.38645.
[27] K.R. Paton, E. Varrla, C. Backes, R.J. Smith, U. Khan, A. O'Neill, C. Boland, M. Lotya, O.M. Istrate, P. King, T. Higgins, S. Barwich, P. May, P. Puczkarski, I. Ahmed, M. Moebius, H. Pettersson, E. Long, J. Coelho, S.E. O'Brien, E. K. McGuire, B.M. Sanchez, G.S. Duesberg, N. McEvoy, T.J. Pennycook, C. Downing, A. Crossley, V. Nicolosi, J.N. Coleman, Scalable production of large quantities of defect-free few-layer graphene by shear exfoliation in liquids, Nat. Mater. 13 (2014) 624–630, https://doi.org/10.1038/nmat3944.
[28] C. Penu, G.-H. Hu, A. Fernandez, P. Marchal, L. Choplin, Rheological and electrical percolation thresholds of carbon nanotube/polymer nanocomposites, Polym. Eng. Sci. 52 (2012) 2173–2181, https://doi.org/10.1002/pen.23162.
[29] S. Al Sheheri, Z. Al-Amshany, Q. Sulami, N. Tashkandi, M. Hussein, R. El-Shishtawy, The preparation of carbon nanofillers and their role on the performance of variable polymer nanocomposites, Des. Monomers Polym. 22 (2019) 8–53, https://doi.org/10.1080/15685551.2019.1565664.
[30] Julia King, M. Via, Characterization of Exfoliated Graphite Nanoplatelets/Polycarbonate Composites: Electrical and Thermal Conductivity, and Tensile, Flexural, and Rheological Properties, 2012, https://doi.org/10.1177/0021998311414073 (Accessed 27 July 2020).
[31] A.K. Kota, B.H. Cipriano, M.K. Duesterberg, A.L. Gershon, D. Powell, S. R. Raghavan, H.A. Bruck, Electrical and rheological percolation in polystyrene/MWCNT nanocomposites, Macromolecules 40 (2007) 7400–7406, https://doi.org/10.1021/ma0711792.
[32] A.S. Krieg, J.A. King, D.C. Jaszczak, I. Miskoglu, O.P. Mills, G.M. Odegard, Tensile and conductivity properties of epoxy composites containing carbon black and graphene nanoplatelets, J. Compos. Mater. 52 (2018) 3909–3918, https://doi.org/10.1177/0021998318771460.
[33] J. Li, J.-K. Kim, M. Lung Sham, Conductive graphite nanoplatelet/epoxy nanocomposites: effects of exfoliation and UV/ozone treatment of graphite, Scr. Mater. 53 (2005) 235–240, https://doi.org/10.1016/j.scriptamat.2005.03.034.
[34] S. Pradhan, S. Chattopadhyay, D. Ratna, Graphene nanoplatelets in polychloroprene matrix: an insight to dispersion with a special emphasize to electro-mechanical properties, Polym. Compos. 40 (2019) E1871–E1883, https://doi.org/10.1002/pc.25180.
[35] J. Billaud, F. Bouville, T. Magrini, C. Villevieille, A.R. Studart, Magnetically aligned graphite electrodes for high-rate performance Li-ion batteries, Nat. Energy 1 (2016) 1–6, https://doi.org/10.1038/nenergy.2016.97.
[36] H. Duan, H. Zhu, J. Yang, J. Gao, Y. Yang, L. Xu, G. Zhao, Y. Liu, Effect of carbon nanofiller dimension on synergistic EMI shielding network of epoxy/metal conductive foams, Compos. Part A Appl. Sci. Manuf. 118 (2019) 41–48, https://doi.org/10.1016/j.compositesa.2018.12.016.
[37] J. Jin, X. Wang, M. Song, Graphene-based nanostructured hybrid materials for conductive and superhydrophobic functional coatings, J. Nanosci. Nanotechnol. 11 (2011) 7715–7722, https://doi.org/10.1166/jnn.2011.4730.
[38] J.S. Oh, J.S. Oh, D.I. Sung, G.Y. Yeom, Fabrication of high-performance graphene nanoplatelet-based transparent electrodes via self-interlayer-exfoliation control, Nanoscale 10 (2018) 2351–2362, https://doi.org/10.1039/C7NR08078F.
[39] X. Wei, D. Li, W. Jiang, Z. Gu, X. Wang, Z. Zhang, Z. Sun, 3D printable graphene composite, Sci. Rep. 5 (2015), https://doi.org/10.1038/srep11181.
[40] T. Wu, E. Gray, B. Chen, A self-healing, adaptive and conductive polymer composite ink for 3D printing of gas sensors, J. Mater. Chem. C 6 (2018) 6200–6207, https://doi.org/10.1039/C8TC01092G.
[41] S. Prolongo, R. Moriche, A. Jimenez-Suarez, M. Sanchez, A. Urena, Advantages and disadvantages of the addition of graphene nanoplatelets to epoxy resins, Eur. Polym. J. 61 (2014) 206–214. https://doi.org/10.1006/j.europolymj.2014.09.022.
[42] J.J. Fallon, S.H. McKnight, M.J. Bortner, Highly loaded fiber filled polymers for material extrusion: a review of current understanding, Addit. Manuf. 30 (2019) 100810, https://doi.org/10.1016/j.addma.2019.100810.
[43] D. Jiang, D.E. Smith, Anisotropic mechanical properties of oriented carbon fiber filled polymer composites produced with fused filament fabrication, Addit. Manuf. (2017) 84–94, https://doi.org/10.1016/j.addma.2017.08.006.
[44] S. Wu, R.B. Ladani, J. Zhang, E. Bafekrpour, K. Ghorbani, A.P. Mouritz, A. J. Kinloch, C.H. Wang, Aligning multilayer graphene flakes with an external electric field to improve multifunctional properties of epoxy nanocomposites, Carbon 94 (2015) 607–618, https://doi.org/10.1016/j.carbon.2015.07.026.
[45] L. Botta, R. Scaffaro, F. Sutera, M.C. Mistretta, Reprocessing of PLA/graphene nanoplatelets nanocomposites, Polymers 10 (2018) 18, https://doi.org/10.3390/polym10010018.

[46] W. Xu, S. Jambhulkar, R. Verma, R. Franklin, D. Ravichandran, K. Song, In situ alignment of graphene nanoplatelets in poly(vinyl alcohol) nanocomposite fibers with controlled stepwise interfacial exfoliation, Nanoscale Adv. (2019) 2510–2517.
[47] S.G. Prolongo, A. Jimenez-Suarez, R. Moriche, A. Ureña, In situ processing of epoxy composites reinforced with graphene nanoplatelets, Compos. Sci. Technol. 86 (2013) 185–191, https://doi.org/10.1016/j.compscitech.2013.06.020.
[48] W. Zhao, H. Wang, H. Tang, G. Chen, Facile preparation of epoxy-based composite with oriented graphite nanosheets, Polymer 47 (2006) 8401–8405, https://doi.org/10.1016/j.polymer.2006.09.025.
[49] Y. Jia, H. He, Y. Geng, B. Huang, X. Peng, High through-plane thermal conductivity of polymer based product with vertical alignment of graphite flakes achieved via 3D printing, Compos. Sci. Technol. 145 (2017) 55–61, https://doi.org/10.1016/j.compscitech.2017.03.035.
[50] Kojima, Novel preferred orientation in injection-molded nylon 6-clay hybrid, J. Polym. Sci. Part B: Polym. Phys. (1995), https://doi.org/10.1002/polb.1995.090330707 (Accessed 27 July 2020).
[51] M. Okamoto, P.H. Nam, P. Maiti, T. Kotaka, N. Hasegawa, A. Usuki, A house of cards structure in polypropylene/clay nanocomposites under elongational flow, Nano Lett. 1 (2001) 295–298, https://doi.org/10.1021/nl0100163.
[52] M. Okamoto, P.H. Nam, P. Maiti, T. Kotaka, T. Nakayama, M. Takada, M. Ohshima, A. Usuki, N. Hasegawa, H. Okamoto, Biaxial flow-induced alignment of silicate layers in polypropylene/clay nanocomposite foam, Nano Lett. 1 (2001) 503–505, https://doi.org/10.1021/nl010051+.